nature communications

Article

https://doi.org/10.1038/s41467-024-51120-3

High-performance Mg_3Sb_2-based thermoelectrics with reduced structural disorder and microstructure evolution

Received: 1 May 2024

Accepted: 31 July 2024

Published online: 09 August 2024

Check for updates

Longquan Wang[1,2], Wenhao Zhang[1], Song Yi Back[1], Naoyuki Kawamoto[3], Duy Hieu Nguyen[3] & Takao Mori[1,2]

Mg_3Sb_2-based thermoelectrics show great promise for next-generation thermoelectric power generators and coolers owing to their excellent figure of merit (zT) and earth-abundant composition elements. However, the complexity of the defect microstructure hinders the advancement of high performance. Here, the defect microstructure is modified via In doping and prolonged sintering time to realize the reduced structural disorder and microstructural evolution, synergistically optimizing electron and phonon transport via a delocalization effect. As a result, an excellent carrier mobility of ~174 $cm^2 V^{-1} s^{-1}$ and an ultralow κ_{lat} of ~0.42 $W m^{-1} K^{-1}$ are realized in this system, leading to an ultrahigh zT of ~2.0 at 723 K. The corresponding single-leg module demonstrates a high conversion efficiency of ~12.6% with a 425 K temperature difference, and the two-pair module of Mg_3Sb_2/MgAgSb displays ~7.1% conversion efficiency with a 276 K temperature difference. This work paves a pathway to improve the thermoelectric performance of Mg_3Sb_2-based materials, and represents a significant step forward for the practical application of Mg_3Sb_2-based devices.

To realize the carbon neutral goal and sustainably developed society, thermoelectric materials represent a potentially helpful technology based on directly converting the waste heat into electricity via solid-state devices[1]. The energy conversion efficiency of the thermoelectric technology is determined by the performance of the thermoelectric materials, a dimensionless figure of merit ($zT = S^2\sigma T/(\kappa_{lat} + \kappa_{ele})$, where S, σ, T, κ_{lat} and κ_{ele} are the Seebeck coefficient, electrical conductivity, absolute temperature, lattice thermal conductivity, and electronic thermal conductivity[2], respectively. However, the widespread application of thermoelectric technology is hindered by the relatively limited thermoelectric performance and scarcity or high cost of materials[3,4]. Pursuing high thermoelectric performance in a material requires optimizing the electrical and phonon transport simultaneously, following the phonon-glass electron-crystal concept[5,6]. Generally, high thermoelectric performance in materials can be achieved by low lattice thermal conductivity, attributed to their complex microstructure, and high electrical transport properties arising from the ordered band structure.

Owing to decades of effort across several strategies, including band structure engineering to enhance electrical transport properties[7–9], and nanostructuring to achieve effective phonon scattering[10–13], high-performance thermoelectric materials with zT_{max} beyond 2.0 have been gradually revealed, such as GeTe[14,15], PbTe[16], $AgSbTe_2$[17], and SnSe[18]. However, all kinds of disadvantages including toxicity, high cost, scarcity, and low stability limit the commercial application of these materials. Recently, there has been a surge of interest in n-type Mg_3Sb_2-based thermoelectric materials because of their promising thermoelectric performance, abundant compositional elements, and cost effectiveness[19,20], which are significant in advancing the applications of thermoelectric technology. Since the report by

[1]Research Center for Materials Nanoarchitectonics (MANA), National Institute for Materials Science (NIMS), Tsukuba, Japan. [2]Graduate School of Pure and Applied Sciences, University of Tsukuba, Tsukuba, Japan. [3]Center for Basic Research on Materials, National Institute for Materials Science (NIMS), Tsukuba, Ibaraki, Japan. e-mail: MORI.Takao@nims.go.jp

Tamaki et al. on n-type Mg_3Sb_2-based alloys with a zT ~ 1.5 at 716 K[21], many of the efforts have been focused on achieving higher performance[22–25], but the progress is limited compared to traditional thermoelectric materials. Therefore, a novel mechanism to realize the high thermoelectric performance in Mg_3Sb_2-based materials is coveted considering the great potential for commercial applications.

The inherent disordered structure with high-density defects in Mg_3Sb_2-based materials limits electron transport with high mobility[26,27]. Recently, the regulation of disorder-induced localization has shown great potential for thermoelectric improvement[17,28], as an effective strategy for changing electron mobility. Based on the relevant physics of Anderson-like electron localization within the parabolic-band-acoustic-phonon-scattering framework, a quantitative transport model predicts that the optimum thermoelectric performance occurs in slightly disordered materials[29]. In the meantime, plentiful microstructural defects contribute to the scattering of phonon transport, thereby leading to the low κ_{lat} in Mg_3Sb_2-based alloys[23,26]. Therefore, the intricate defect microstructure in Mg_3Sb_2-based alloys indicates the prospect of improving electron transport and restraining phonon transport by combining disorder-induced localization and nanostructuring engineering to advance thermoelectric performance.

Herein, the reduced structural disorder in Mg_3Sb_2-based alloys is realized by introducing In doping, coupled with the synergetic microstructure evolution for phonon scattering through prolonged sintering time. The reduced structural disorder promotes electron transport, benefiting from the transition of electron localization to delocalization, synergistically reducing grain boundary scattering, so the excellent carrier mobility of ~174 $cm^2 V^{-1} s^{-1}$ is realized in our sample. Moreover, the reconstructed defect microstructure facilitates multiple strain fluctuations, thereby restraining phonon transport, leading to an ultralow κ_{lat} of ~0.42 $W m^{-1} K^{-1}$ in our $Mg_{3.2}In_{0.005}Sb_{1.5}Bi_{0.49}Te_{0.01}$ sample. The significantly improved thermoelectric performance shows the zT with ~0.5 at room temperature to ~2.0 at 723 K (Fig. 1a), which is one of the best values reported in Mg_3Sb_2-based alloys[21–24,30,31]. As a result, a high average zT of ~1.36 in the temperature range of 300–723 K is achieved in our sample (Fig. 1b). The excellent thermoelectric performance, especially the high average zT, is the foundation for the application to pursue a high conversion efficiency of the modules. Therefore, the corresponding fabricated single-leg module shows an exceptionally high conversion efficiency of ~12.6% with a temperature difference of 425 K, which is the superior value among known n-type single-leg modules in this applicatively important temperature range (Fig. 1c)[32–37]. Subsequently, the optimized n-type materials are fabricated into a two-pair module coupled with a p-type MgAgSb compound. The fabricated two-pair module demonstrates a high conversion efficiency of ~7.1% with a temperature difference of 276 K for power generation, which is challenging with the low-temperature monopoly of Bi_2Te_3 (Fig. 1d)[38–40]. Therefore, our Mg_3Sb_2-based alloys demonstrate great progressiveness and application potential in a wide temperature range due to the simultaneous control of electron and phonon transport.

Results

To explore the origin of the high performance, the electrical properties of our samples were systematically investigated. The thermally activated conductivity normally occurs in the n-type Mg_3Sb_2-based materials, which limits low-temperature σ and zT. This temperature-dependent tendency of σ was found in the $x = 0$–10 min sample (Fig. 2a), which was ascribed to the electron scattering derived from grain boundaries and defects[27,41,42]. Interestingly, the near-room-temperature σ was significantly improved via minor In doping

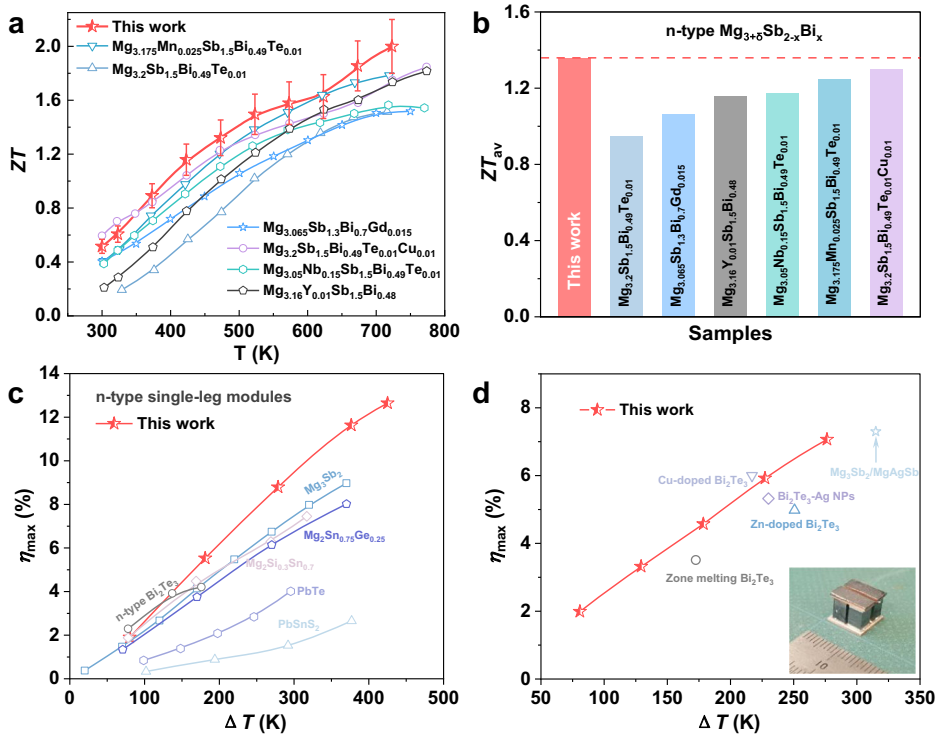

Fig. 1 | High performance of the Mg_3Sb_2-based thermoelectric materials and modules. a Temperature-dependent zT, and (**b**) average zT within 300–723 K of the sample in this work with a comparison to literature results for Mg_3Sb_2-based materials[21–24,30,31]. **c** Maximum conversion efficiency as a function of ΔT for the single-leg module in this work, in comparison with known n-type single-leg modules[32–37]. **d** Comparison of the maximum conversion efficiency of the two-pair module in this work with Bi_2Te_3-based[38–40] and Mg-based[22] modules. The error bar represents the uncertainty of the measurement result.

https://doi.org/10.1038/s41467-024-51120-3

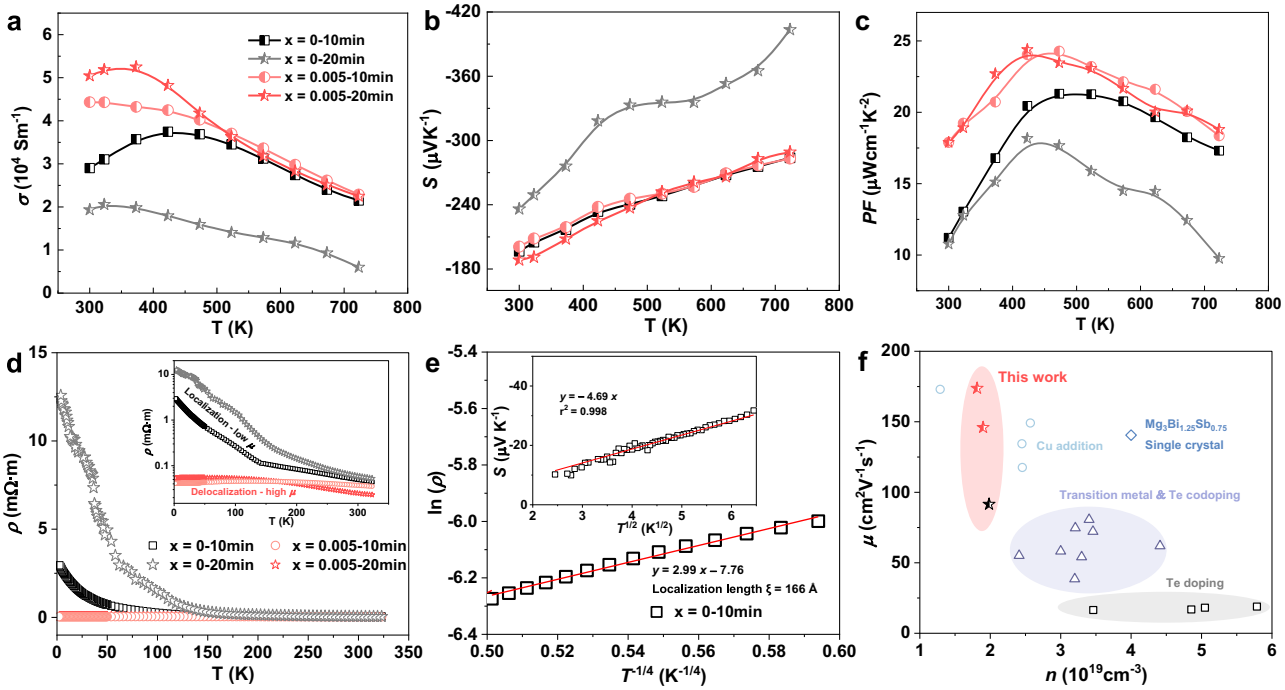

Fig. 2 | Electrical transport properties. Temperature-dependent (**a**) electrical conductivity, (**b**) Seebeck coefficient, (**c**) power factor of the $Mg_{3.2}In_xSb_{1.5}Bi_{0.49}Te_{0.01}$ samples. **d** Low-temperature electrical resistivity of the samples, and the inset shows the enlarged details by the logarithmic axis. **e** ln ρ versus $T^{-1/4}$ and S versus $T^{1/2}$ plots. The variable-range hopping (VRH) behavior in the sample with the evidences from electrical resistivity and Seebeck coefficient. **f** The relationship between Hall carrier concentration and mobility for the samples in this work and reported values in the Mg_3Sb_2-based system[22–25,51,52].

($x = 0.005$–10 min), as shown in Fig. 2a. Our previous research and related literatures have proved the important effect of grain boundaries on electron transport[27,42–44]. In addition, defect-dominated electron scattering, such as Mg vacancies and interstitials, in Mg_3Sb_2-based materials cannot be completely ignored, and the appreciable role in electron scattering of the point defects has been recently highlighted by Zhang et al.[27]. Therefore, the potential possibility for the improved low-temperature σ here may stem from reduced electron scattering by grain boundaries and defects.

We tried applying a prolonged sintering time to our samples, which led to a further improvement of σ in the low-temperature range of $x = 0.005$–20 min sample. It can be ascribed to the reduced grain boundary scattering by prolonging the sintering time, because the higher sintering temperature and longer holding time can promote grain growth driven by thermodynamics. However, the undoped sample has an apparently deteriorative σ due to the unavoidable Mg loss during high-temperature sintering, which is evident from the porous structure observed in the fracture morphology of $x = 0$–20 min sample (Supplementary Fig. 1). Supplementary Fig. 2 shows the X-ray diffraction (XRD) patterns of our samples with different In doping and sintering time, and all the samples can be indexed to the Mg_3Sb_2 phase. Additionally, the XRD pattern of the melting phase during high-temperature sintering was detected, confirming the existence of Mg evaporation during the high-temperature spark plasma sintering (SPS) process. According to the phase boundary mapping[45], the excess Mg is crucial for achieving the n-type behavior in Mg_3Sb_2-based alloys and exerts a significant influence on the thermoelectric performance. Therefore, the electrical properties of the $x = 0$–20 min sample sharply deteriorated due to heavily reduced carrier concentration (Fig. 2a, b and Supplementary Table 1). However, this adverse Mg loss has been suppressed after In doping, so the $x = 0.005$–20 min sample shows the improved σ and also comparable S compared to the $x = 0$–10 min sample. To explore this pattern, we prepared samples with different In doping and sintering time (Supplementary Figs. 3–7), and the ratio of σ for different samples was used to distinguish the degree of performance deterioration (Supplementary Fig. 8). The ratio for the undoped sample is significantly lower than that for the In-doped samples. The trend in the ratios of σ_{20}/σ_{10} and σ_{30}/σ_{10} suggests improved stability in In-doped samples during high-temperature sintering compared to undoped samples, which might originate from the apparent higher atomic mass and stability of In compared to Mg. Moreover, the inductively coupled plasma atomic emission spectroscopy (ICP-OES) was performed to check the actual composition of our samples, confirming minor In doping and effectively restrained Mg evaporation during the sintering after In doping (Supplementary Table 2). As a result, no noticeable changes in composition were found in our In-doped samples, even with prolonged sintering times. In addition, minor In doping ($x = 0.005$) was applied in further research based on the optimized weighted mobility, but increased In content would cause a slightly decreased low-temperature σ due to additional electron scattering from the Mg-rich phase (Supplementary Fig. 7)[46]. Therefore, the In-doped samples obtained observably improved power factor (*PF*) owing to increased σ, especially in the low-temperature range (Fig. 2c). The room-temperature *PF* increases from 11.20 μW cm^{-1} K^{-2} for the $x = 0$–10 min to 17.90 μW cm^{-1} K^{-2} for the $x = 0.005$–20 min sample.

To reveal the origin of this extraordinary improvement in electrical properties, we measured the low-temperature (2–323 K) electrical resistivity of our samples (Fig. 2d). As a result, we observed a transition from insulating behavior to metallic behavior upon In-doping. Apparently, the In-free samples exhibit a sharp increase in resistivity below 50 K, which indicates the charge carrier localization, in line with disorder-induced charge localization (i.e., Anderson localization)[28,29]. Conversely, a semiconductor-like transport in the resistivity was found in the In-doped samples. At sufficiently low temperatures, in disordered materials, the electronic transport

mechanism relies on the hopping conduction between localized electronic states near the Fermi level. Therefore, the low-temperature resistivity in the disordered system can be understood via variable range hopping (VRH) conduction[47]:

$$\rho(T) = \rho_0 \exp\left[\left(\frac{T_0}{T}\right)^{\frac{1}{d+1}}\right] \quad (1)$$

where ρ_0 and T_0 are the pre-factor of electrical resistivity and characteristic temperature, respectively. The value of the exponent, $1/(d+1)$, is given to be 1/4 by Mott VRH hopping in three-dimensional systems. In the VRH system, the T_0 inversely depends on the localization length ξ with the relationship of $k_B T_0 = 18.1/[D(E_F)\xi^3]$[48], which diverges with the insulator-metal transition. The k_B, $D(E_F)$ are the Boltzmann constant and density of states at Fermi level energy, respectively. It is confirmed that the undoped samples experience unavoidable Mg loss, and the induced defects can play a role as a random source of disorder. Therefore, we have plotted the electrical resistivity of the undoped samples (x = 0–10 min, x = 0–20 min) by using VRH conduction, which shows good fitting, as shown in Fig. 2e and Supplementary Fig. 9a. According to the criterion of Mott VRH hopping conduction, the average hopping distance R_M must be larger than the localization length ξ, $R_M/\xi = (3/8)(T_M/T)^{1/4} > 1$, with the undoped sample following this criterion well. Hence, it can be concluded that the insulating behavior of undoped samples below 50 K is caused by the charge carrier localization induced by disorder. T_0 was obtained by fitting lnρ versus $T^{-1/4}$ (Fig. 2e), and $D(E_F)$ was estimated using low-temperature specific heat (Supplementary Fig. 10). The detailed physical parameters for this fitting are listed in Supplementary Table 3. A localization length of 166 Å was obtained for the x = 0–10 min sample. The value of localized length is much larger than the lattice constant, indicating the Anderson weak localization in the undoped sample. Strikingly, it can be observed that the localized charge carrier is delocalized through In doping, as shown in Fig. 2d. This suggests that In doping successfully prevents the formation of the disordered structure caused by Mg defects during high-temperature sintering, leading to improved electronic transport properties. Therefore, the ultra-low carrier mobility has been demonstrated in the pristine sample compared to the In-doped sample at low temperatures (10 K and 50 K) due to the charge localization, as shown in Supplementary Fig. 9b. Furthermore, the low-temperature S deviates from the simple linear temperature-dependent behavior, but follows a relationship of S versus $T^{1/2}$, consistent with VRH in three-dimensional systems, confirming the Mott VRH conduction (Fig. 2e)[49,50]. Benefiting from the transition from charge localization in undoped samples to delocalization in In-doped samples, coupled with slightly reduced grain boundary scattering, we achieved a more than 90 % enhancement in carrier mobility at room temperature, reaching a record value of 174 $cm^2 V^{-1} s^{-1}$ in x = 0.005–20 min sample (Fig. 2f), surpassing those of polycrystalline and even single-crystal samples[22–25,51,52]. In addition, the slightly decreased carrier concentration in the In-doped samples may be caused by the charge compensation effect due to different substitutional positions[53].

To trace the source of the disorder-induced localization in Mg_3Sb_2-based alloys, it is possible that, Frenkel defects, consisting of Mg vacancies and interstitials, could be responsible for creating the heavily disordered structure. The crystal structure of Mg_3Sb_2 consists of a tetrahedrally coordinated anion $[Mg_2Sb_2]^{2-}$ layer and an octahedrally coordinated cation Mg^{2+} layer stacked in the z direction[19]. Therefore, the structure contains two Mg positions, and the refined occupancy parameter at Mg (1) sites (octahedral site) was utilized to validate vacancy generation, as evidenced by synchrotron powder X-ray diffraction (XRD) measurement in previous literatures[26,27]. The high-energy and high-sensitive XRD measurements were conducted on our samples to confirm this defect structure (Supplementary Fig. 11), and detailed Rietveld-refined parameters are shown in Supplementary Tables 4–6. The vacancy generation was confirmed by the refined occupancy of the Mg (1) site, ~0.928 for the x = 0–10 min and ~0.938 for the x = 0.005–20 min sample, indicating the existence of the Mg vacancies and interstitial. Moreover, the slightly higher occupancy in the x = 0.005–20 min sample demonstrates the effective suppression of Mg loss by In doping, consistent with the previous discussion on electrical properties. In addition, the apparent higher electrical resistivity observed in the x = 0–20 min sample at low temperatures indicates the stronger disorder-induced localization (Fig. 2d), likely caused by the high-density random defects by Mg evaporation during high-temperature sintering. This reaffirms the potential relationship between Frenkel defects and disordered structure. Therefore, improving electrical properties at low temperatures can be achieved by reducing structural disorder, confirming the appreciable role of defects in the electron transport of n-type Mg_3Sb_2-based materials.

To investigate the effect of grain boundary scattering in our samples, electron backscatter diffraction (EBSD) was utilized to measure the grain sizes (Fig. 3a, b). A slightly increased average grain size, from 4.4 μm for the pristine sample to 5.6 μm for the In-doped sample, was observed (Supplementary Fig. 12), which contributes to the enhanced electrical transport. This increase may be attributed to the reduced solute dragging effect from Mg and Bi on grain boundary migration[54,55], resulting in slightly promoted grain growth. To explore the microstructural evolution, transmission electron microscopy (TEM) observations were performed on the x = 0–10 min and x = 0.005–20 min samples. Random nanoprecipitates (blue circle) and Moiré fringes (yellow circle) were observed in the x = 0–10 min sample, as depicted in Fig. 3c and Supplementary Fig. 13. The presence of nanoprecipitates may be associated with composition fluctuations in n-type Mg_3Sb_2, and previous reports have identified nanometer-scale Bi-rich phases using TEM and atom probe tomography[56,57]. In addition, the Moiré fringe, originating from the overlapping of two lattices with comparable periodic spacing, has been demonstrated for qualitative analysis of defect and strain in TEM[58,59]. The corresponding selected area electron diffraction (SAED) pattern reveals the misoriented angle between the overlapped lattice grating, allowing for the indication of randomly distributed defects in x = 0–10 min sample by the Moiré fringe, typically accompanied by high-density lattice defects[58]. The apparent lattice distortion has been observed to alleviate the lattice strain caused by existing defect structures in the sample (red rectangle). However, the microstructure of x = 0.005–20 min sample exhibits a distinctly different arrangement, characterized by collective nanoprecipitates and Moiré fringes, as illustrated in Fig. 3d and Supplementary Fig. 14. The lattice distortion induced by nanoprecipitates and dislocations around the edges of the Moiré fringe serves as scattering centers, impeding phonon propagation (Fig. 3e–h). Simultaneously, strong lattice distortion has been found in the x = 0.005–20 min sample, with corresponding geometric phase analysis (GPA) revealing intense strains in this region (Fig. 3i, j and Supplementary Fig. 14)[60]. The strain fluctuation region should be caused by the high-concentration defect structures observed in the x = 0.005–20 min sample characterized by TEM images. A typical Williamson-Hall analysis was conducted for quantitative analysis of lattice strain in our samples (Supplementary Fig. 15). It reveals an increasing trend of lattice strain attributed to the microstructural evolution following In doping and prolonged sintering time, consistent with TEM observations and GPA analysis. This

https://doi.org/10.1038/s41467-024-51120-3

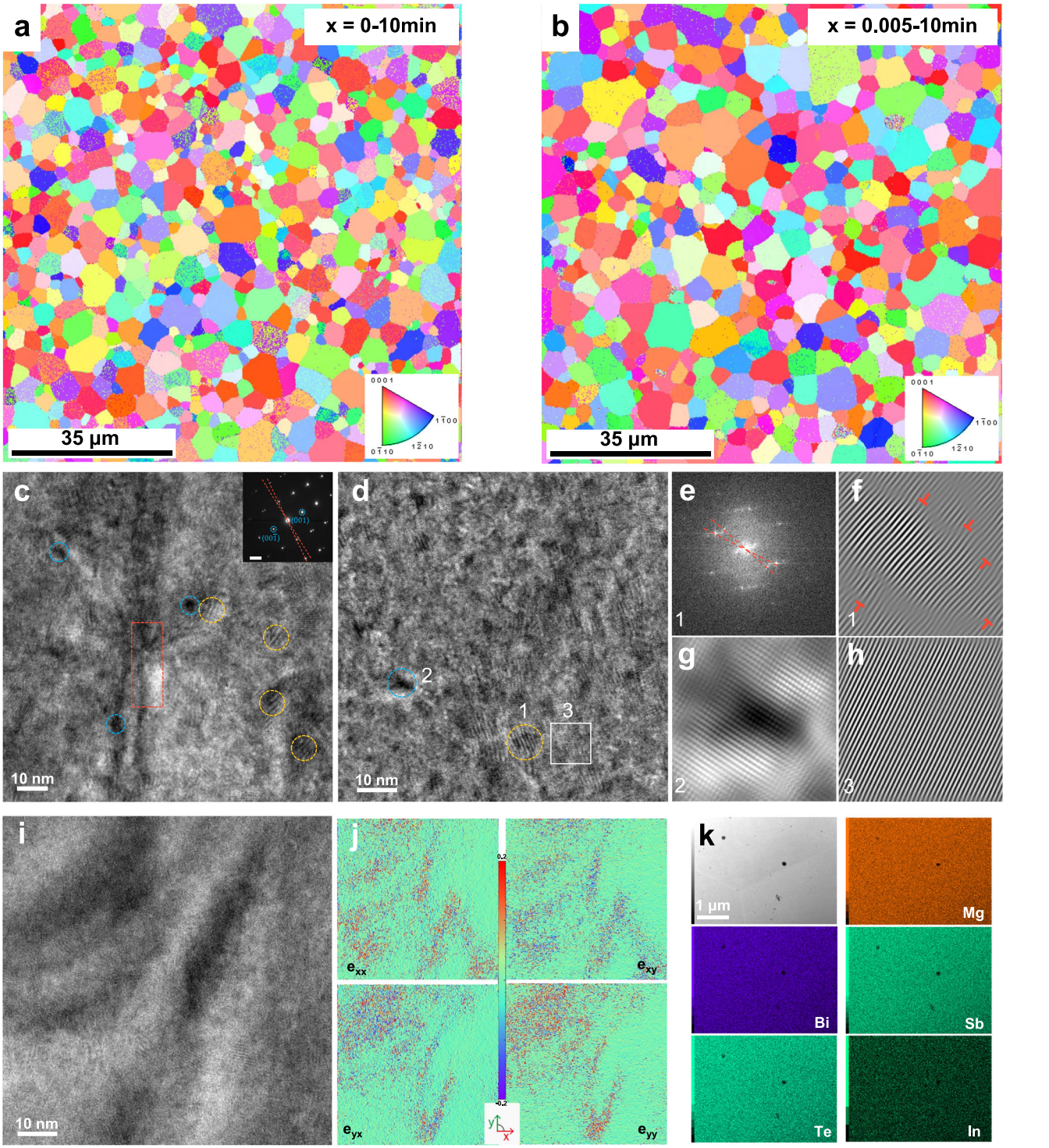

Fig. 3 | Microstructural evolution induced by In doping and prolonged sintering time. Electron backscatter diffraction (EBSD) crystal-orientation maps of (**a**) $x = 0$–10 min, (**b**) $x = 0.005$–10 min samples. Transmission electron microscopy (TEM) lattice image of (**c**) $x = 0$–10 min, (**d**) $x = 0.005$–20 min samples, and the inset of (**c**) reveals the corresponding selected-area electron diffraction (SEAD) pattern. The high-density nanoprecipitates (blue circle), Moiré fringe (yellow circle) and lattice distortion (red rectangle) are observed in the samples. **e**, **f** Fast Fourier transform (FFT) and inverse FFT images of the selected Moiré fringe regions 1 in **d**. Inverse FFT images of the (**g**) nanoprecipitate region 2, (**h**) perfect-lattice region 3 in **d**. **i** TEM image with obvious lattice distortion for the $x = 0.005$–20 min sample and (**j**) corresponding strain maps along different directions. **k** HAADF-STEM image showing the clean triple-junction of the grain boundary and corresponding EDS element mapping images.

microstructural evolution results in the apparent higher strain fluctuation in the samples, which is a crucial factor for restraining phonon transport. Additionally, a high-angle annular dark-field scanning TEM (HAADF-STEM) image reveals a neat triple-junction of the grain boundary in the $x = 0.005$–20 min sample (Fig. 3k), supporting that the In doping does not function via grain boundary segregation, highlighting a distinction between this work and previous common grain boundary segregation research[42,61].

https://doi.org/10.1038/s41467-024-51120-3

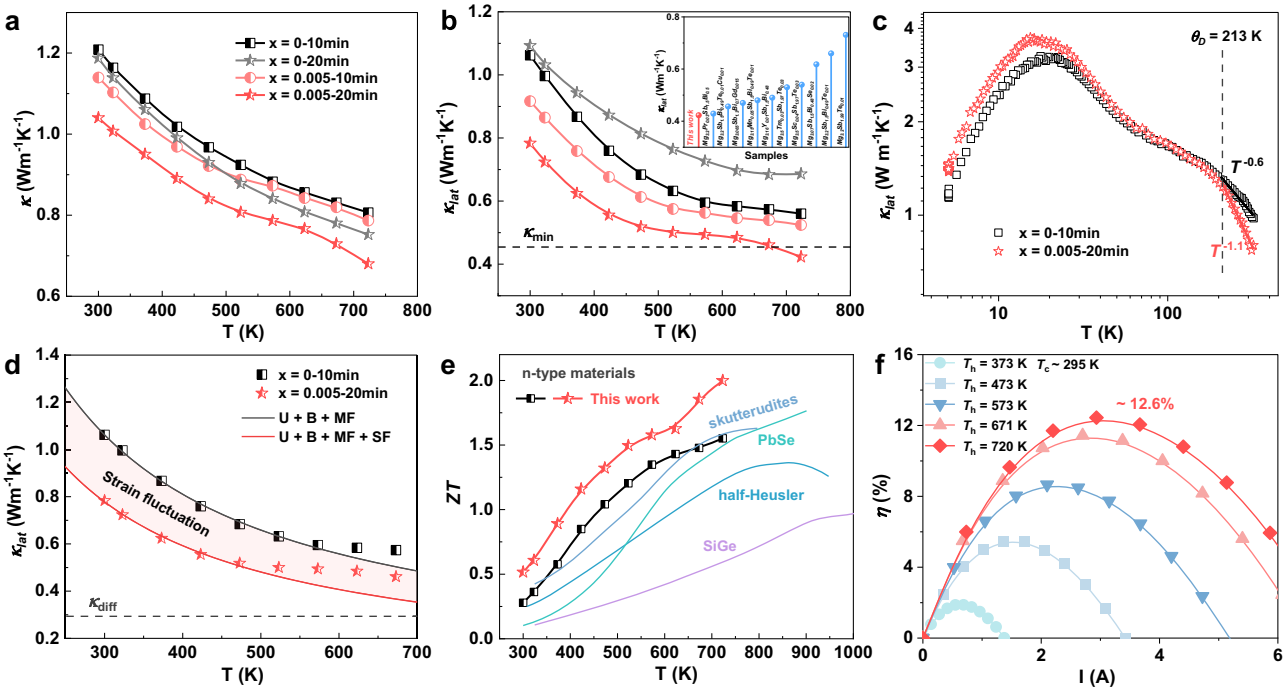

Fig. 4 | Thermoelectric properties of the materials and module. Temperature-dependent (**a**) thermal conductivity, (**b**) lattice thermal conductivity of the $Mg_{3.2}In_xSb_{1.5}Bi_{0.49}Te_{0.01}$ samples. The inset compares the minimum lattice thermal conductivity in this work and reported values for Mg_3Sb_2-based alloys[21–23,30,31,51,63–66]. **c** Low-temperature lattice thermal conductivity. **d** Experimental and calculated lattice thermal conductivity of the samples, considering Umklapp process (U), grain boundaries (B), mass fluctuation (MF) and strain fluctuation (SF). **e** Temperature-dependent zT of the samples in this work, in comparison with state-of-the-art n-type thermoelectric materials[13,78–80]. **f** Maximum conversion efficiency as a function of the current under different hot-side temperatures for the single-leg module.

Figure 4a displays the κ of the samples, and the notably lower κ happened in the $x = 0.005$–20 min sample. By subtracting the κ_{ele} from the κ, where the κ_{ele} is calculated as $L\sigma T$ ($L = 1.5 + \exp(-|S|/116)$[62], the κ_{lat} was determined to evaluate phonon transport (Fig. 4b). The sample with In doping ($x = 0.005$–10 min) demonstrates a lower κ_{lat} compared to the undoped sample, and the $x = 0.005$–20 min sample further reduces κ_{lat} across the entire temperature range. For instance, the room-temperature κ_{lat} reduces from 1.06 W m^{-1} K^{-1} for the pristine sample to 0.78 W m^{-1} K^{-1} for the $x = 0.005$–20 min sample. It reaches the minimum value of ~0.42 W m^{-1} K^{-1} at 723 K for the $x = 0.005$–20 min sample, which is lower than that of all other doped Mg_3Sb_2-based alloys (Fig. 4b)[21–23,30,31,51,63–66]. Moreover, the high-temperature κ_{lat} falls below the minimum value predicted by the Cahill model and approaches the diffusion limit proposed by Snyder et al.[67,68]. It should be noted that the abnormally increased κ_{lat} in the $x = 0$–20 min sample is attributed to the destructive microstructure due to the Mg evaporation. Therefore, the apparent reduction in κ_{lat} in our sample should be ascribed to the microstructural evolution induced by In doping and prolonged sintering time as discussed before.

The low-temperature κ_{lat} displays typical characteristics of the polycrystal materials in the temperature of 5–323 K (Fig. 4c)[69]. Initially, the κ_{lat} increase with temperature as $\kappa_{lat} \sim T^n$ due to the gradually excitation of acoustic phonons. Later, the maximum κ_{lat} occurs where the phonon mean free path controlled by defects is comparable to the phonon-phonon scattering processes. The $x = 0.005$–20 min sample has a peak κ_{lat} of 3.74 W m^{-1} K^{-1} at 15 K, which is similar to the previous report in polycrystalline Mg_3Sb_2[26]. With the increase in temperature, κ_{lat} decreases due to the stronger phonon-phonon scattering process and shows a different temperature dependence at $T > \theta_D$. Klemens-Callaway's model provides a method to analyze the κ_{lat} of defect-containing crystalline solids at high temperatures ($T > \theta_D$)[70,71].

$$\kappa_{lat} = \frac{k_B}{2\pi^2 v_s (ACT)^{\frac{1}{2}}} \tan^{-1}\left(\frac{k_B\theta}{\hbar}\left(\frac{A}{CT}\right)^{\frac{1}{2}}\right) = \frac{k_B\sqrt{v_s}}{\sqrt{\pi^3}} \frac{1}{\sqrt{\Omega_0 C\Gamma}} \frac{1}{\sqrt{T}} \tan^{-1}\left(\frac{k_B\theta}{\hbar}\left(\frac{\Omega_0\Gamma}{4\pi v_s^3 CT}\right)^{\frac{1}{2}}\right) \quad (2)$$

where Ω_0 is the unit cell volume, C is the inverse time coefficient for phonon-phonon scattering processes in the pure and perfect materials, and Γ is the point defect scattering strength parameter determined by the fractions and types of the defects. The expression for A is $A = \frac{\Omega_0\Gamma}{4\pi v_s^3}$ given by Klemens. In the case of large defect scattering for solid solutions, the term of $\tan^{-1}(\frac{k_B\theta}{\hbar}(\frac{A}{CT})^{1/2}) \approx \pi/2$, so the formula can be rewritten as $\kappa_{lat} = \frac{k_B}{4\pi v_s (ACT)^{1/2}}$. Therefore, the κ_{lat} has a temperature dependence of $T^{-1/2}$, close to the trend observed for the $x = 0$–10 min sample of $T^{-0.6}$ (Fig. 4c). This moderate temperature dependence of κ_{lat} was also observed in previously reported Mg_3Sb_2-based alloys[26], indicating the presence of disordered structure with high-density defects as discussed before. However, the κ_{lat} for the $x = 0.005$–20 min sample displays a stronger temperature dependence of $T^{-1.1}$, leading to the lower κ_{lat} in the sample compared to the pristine sample. This variation can be understood via the competing mechanism between the phonon-phonon and phone-defect scattering. Point defects show a strong suppressed effect on the temperature dependence, even for extremely low defect fractions[72]. Therefore, the plentiful Mg vacancies in pristine sample result in the moderate temperature dependence due to the competition between intrinsic and extrinsic phonon scattering. The reduced

Mg vacancies and structural disorder via defect evolution in our In-doped sample suppress the phonon-defect scattering effect, leading to an increased temperature dependence of κ_{lat}. To better understanding the stronger temperature dependence in $x = 0.005$–20 min sample, the linear thermal expansion of the samples was explored (Supplementary Fig. 16). The large coefficient of linear thermal expansion in our sample (~21.2×10^{-6} K^{-1}), comparable with anharmonic materials such as PbTe and SnTe[73], indicates stronger phonon anharmonicity. Previous work systematically investigated the anomalous low thermal conductivity in Mg_3Sb_2, revealing higher thermal expansion in Mg_3Sb_2 compared to isostructural compounds ($CaMg_2Sb_2$, $YbMg_2Sb_2$)[74]. This suggests that highly anharmonic acoustic branches contribute to the low thermal conductivity. Additionally, the inherently low lattice thermal conductivity in Mg_3Sb_2 has been attributed to phononic origins[75], underscoring the importance of controlling phonon-phonon interaction to reduce lattice thermal conductivity. Therefore, the transition from charge localization to delocalization via defect regulation in our work may weaken the suppression of temperature dependence from phonon-defect scattering, thus leading to the lower lattice thermal conductivity based on high phonon anharmonicity. Noticeably, the Klemens-Callaway model is limited in describing the high-temperature κ_{lat}, as it suggests that κ_{lat} decreases endlessly with temperature, whereas materials eventually reach saturation at a constant value. Next, the Debye-Callaway model was adopted to fit the high temperature κ_{lat} of our samples[76], as shown in Fig. 4d. The detailed calculation and parameters can be found in the supplementary materials. The Umklapp process (U), grain boundaries (B), mass fluctuation (MF) and strain fluctuation (SF) were considered as the source of phonon scattering and their contributions were fitted to our experimental data. Figure 4d shows the fitted results for the samples, and the apparent reduction in κ_{lat} for the $x = 0.005$–20 min sample compared to the pristine sample is found to be caused by the stronger strain fluctuation resulting from microstructural evolution, which was verified by previous Williamson-Hall and GPA analysis. Additionally, it has been reported that lattice strain can suppress the insulating Mott phase and induce a transition to metallic behavior[77]. This transition from insulator to metal due to lattice strain further supports our analysis of electrical resistivity at low temperatures. The introduction of In doping not only promotes charge delocalization, enhancing carrier mobility, but also induces fluctuations in lattice strain, consequently reducing lattice thermal conductivity. Moreover, the broadening of the Raman spectrum indicates a shorter phonon relaxation time and stronger phonon scattering in the $x = 0.005$–20 min sample (Supplementary Fig. 17).

Benefiting from the improved electron transport and effectively restrained phonon transport, the significantly enhanced zT occurs in our samples in the temperature range of 100–723 K (Fig. 4e and Supplementary Figs. 18 and 19). The improved n-type Mg_3Sb_2-based alloys demonstrate excellent thermoelectric performance across the entire temperature range, outperforming most state-of-the-art n-type materials and indicating great potential for power generation applications[13,78–80]. The $x = 0$–10 min sample has a peak zT of 1.55 at 723 K and an average zT of 1.07 in the temperature range of 300–723 K, consistent with previous reports[21,22]. Strikingly, the $x = 0.005$–20 min sample reaches a maximum zT of 2.0 at 723 K and an average zT of 1.36 in the temperature range of 300–723 K, representing an increase of ~29% and ~27% compared to the undoped sample, respectively. High-performance samples were reproduced, and similar properties were measured, demonstrating good reproducibility (Supplementary Fig. 20). We would like to point out that the heat capacity measured by the differential scanning calorimeter (DSC) was applied to estimate the κ and zT of our samples (Supplementary Fig. 21). The maximum zT of our sample could reach ~2.13 at 723 K if we calculate κ based on the heat capacity determined by the Dulong-Petit law (Supplementary Fig. 21). Motivated by the ultra-high zT in the optimized sample, we successfully fabricated a single-leg module with an interface prepared using 304 stainless steel powder and Mg turning to evaluate the energy conversion efficiency[81]. Details regarding the module fabrication and measurement can be found in the methods part. As shown in Figs. 1c and 4f, and Supplementary Fig. 22, a high conversion efficiency of ~12.6% was achieved in the single-leg module with a 425 K temperature difference, which is the superior value among Mg_3Sb_2-based materials. The excellent reproducibility and stability of the single-leg module are demonstrated in Supplementary Fig. 23. Importantly, it stands as the optimum choice for the n-type materials in the low- to mid-temperature range, considering its excellent efficiency and comparatively low cost compared to other common n-type materials. The theoretical efficiency based on finite element simulations reaches ~16%, with the disparity displayed in the internal resistance and heat flow between the measured value and predicted value, indicating the need for further progress to improve the contact layer and thermal radiation evaluation (Supplementary Figs. 24 and 25). Next, the p-type MgAgSb was selected to fabricate the two-pair module due to its comparable mechanical and thermoelectric properties (Supplementary Fig. 26). The contact layer information of the n-type and p-type legs was examined through the scanning electron microscope (SEM) images and corresponding EDS mapping (Supplementary Figs. 27 and 28). Supplementary Figure 29 illustrates the output voltage, output power, heat flow from the cold side, and conversion efficiency as functions of current under various temperature differences. A maximum conversion efficiency of ~7.1% was obtained with a 276 K temperature difference, representing a competing value compared to the Bi_2Te_3-based module[38–40]. However, it is still notably lower than the simulated value, close to ~11%, due to the higher internal resistance and slightly lower open circuit voltage (Supplementary Figs. 30 and 31). This underscores the importance of interface contact to reduce the inevitable contact resistance of electrical and thermal across multiple layers in the device (Supplementary Fig. 32). Additionally, the measured open circuit heat flow is higher than the theoretical value at high-temperature gradients due to the heat radiation from the unfilled part. Dedicated efforts toward interfacial layer design and connection technology are required to achieve higher efficiency in future work. The detailed schematic diagram of the energy conversion efficiency measurement system of Mini-PEM and the simulated temperature distribution are shown in Supplementary Figs. 33 and 34. It is worth emphasizing that the servicing temperature for our module is limited by the phase-transition temperature in p-type MgAgSb (Supplementary Fig. 35), demonstrating the potential to realize higher efficiency coupled with mid-temperature p-type materials. Considering the lower materials cost, better mechanical properties compared to Bi_2Te_3-based materials, and higher stability of Sb-rich Mg_3Sb_2 compared to Bi-rich Mg_3Bi_2, our module shows the competing advantages for harvesting abundant low-grade waste heat.

Discussion

In summary, the reduced structural disorder and enhanced strain fluctuation through microstructural evolution were realized in our sample via In doping and prolonged sintering time, leading to synergistically optimal electron and phonon transport. The excellent carrier mobility of ~174 cm^2 V^{-1} s^{-1} and ultralow κ_{lat} of ~0.42 W m^{-1} K^{-1} occurred in the sample, which leads to superior zT values ranging

from ~0.5 at room temperature to ~2.0 at 723 K in our Mg_3Sb_2-based alloys. Consequently, the fabricated single-leg module demonstrated a high conversion efficiency of ~12.6% with a temperature difference of 425 K, and the two-pair module reached a maximum efficiency of ~7.1% with a temperature difference of 276 K coupled with p-type MgAgSb. Our work would significantly accelerate the progression of n-type Mg_3Sb_2-based alloys and highlight the bright application potential for thermoelectrics in low- to mid-temperature energy harvesting.

Methods

Synthesis process

To prepare the samples of $Mg_{3.2}In_xSb_{1.5}Bi_{0.49}Te_{0.01}$, the high-purity raw materials of Mg (99.95%), Te (99.999%), Bi (99.999%), Sb (99.999%), and In (99.99%) were stoichiometrically weighted and then loaded into the stainless-steel ball milling jaw in the glovebox for high-energy milling process. The ball-milling process was kept for 5 hours and then was consolidated by spark plasma sintering (SPS, SPS-1080 System, SPS SYNTEX INC) under axial pressure of 60 MPa at 700 °C. The sintering time for SPS is 10 min, 20 min, and 30 min to prepare different samples, which are labeled as x–10min, x–20min, and x–30min. The sample of p-type $Mg_{0.995}In_{0.005}Ag_{0.97}Sb_{0.99}$ was prepared via a two-step ball-milling process. The raw materials of Mg (99.95%) and Ag (99.99%) were stoichiometrically weighted and then loaded into the stainless-steel ball milling jaw in the glovebox for the high-energy milling process. The first-step ball-milling process is 10 hours and then add Sb (99.999%), In (99.99%) to finish the second-step ball-milling with 5 hours. The obtained powder was consolidated by SPS at 573 K with 60 MPa for 5 min.

Properties characterization

The prepared samples were cut into strips and columns for measuring electrical and thermal properties. The electrical properties of σ and S were measured by the ZEM-2 instrument in a helium atmosphere (ADVANCE RIKO, ±5% uncertainty). The thermal conductivity κ was calculated using the equation $\kappa = \lambda C_p d$, where the thermal diffusivity λ was measured by a laser flash method (LFA 467, NETZSCH, ±3% uncertainty), the densities d was measured by an Archimedes method. The heat capacity C_p was measured by the differential scanning calorimeter (DSC) measurement (Netzsch STA 449F1 Jupiter) in an N_2 atmosphere at a heating rate of 5 K/min. The Hall carrier concentration was measured using a Physical Properties Measuring Systems (PPMS, Quantum Design). The PPMS with an AC resistance option was applied to measure low-temperature (2–323 K) resistivity, a thermal transport option was also used to measure the low-temperature (5–323 K) thermoelectric properties of σ, S and κ in the same direction, and a heat capacity option was used to perform low-temperature (2–300 K) heat capacity.

Phase and microstructure characterization

The XRD patterns were measured using the X-ray diffractometer (MiniFlex600-Cu, Rigaku) with Cu Kα radiation operating at 40 kV × 15 mA, and the scanning rate was set as 3°/min. The high-energy and high-sensitivity type XRD was performed by SmartLab 9 kW (Rigaku) with Cu Kα radiation operating at 45 kV × 200 mA, and the corresponding data was used to do Rietveld refinement. Electron backscattered diffraction (EBSD) measurements were performed using a FE-SEM (JSM-7001F, JEOL Ltd.) operated at 15 kV with a step size of 0.2 μm. The samples for EBSD observation were prepared by mechanical polishing to 0.1 μm with diamond paste and then ion milling. The micro-Raman was carried out using a laser confocal microscope (inVia, Renishaw) with a 532 nm excitation laser and an electron multiplying CCD detector. The fracture structure and composition were characterized using a scanning electron microscope (FESEM, Hitachi SU8000) equipped with an energy dispersive spectrometer (EDS, XFlash FlatQUAD 5060 F). The microstructure was carried out by a transmission electron microscopy (TEM, JEOL JEM-3100FEF) at an acceleration voltage of 300 kV with a STEM mode equipped with an EDS detector. TEM samples were prepared by the focused ion beam (FIB) method with Ar milling. Longitudinal (v_l) and transverse (v_t) sound velocity was measured by using a sing-around ultrasonic velocity measuring instrument (UVM-2, Ultrasonic Engineering Co., Ltd) at room temperature, and corresponding average sound velocity (v) was calculated via the equation: $\nu^{-3} = \frac{1}{3}(\nu_l^{-3} + 2\nu_t^{-3})$. The linear thermal expansion was measured using a dilatometer in an Ar atmosphere at a heating rate of 5 K/min (Netzsch DIL 402c). The actual composition of the samples was determined by inductively coupled plasma atomic emission spectrometer (720 ICP-OES, Agilent Technologies Japan, Ltd.).

Module fabrication and efficiency evaluation

To fabricate the single-leg module, the interface material and $Mg_{3.2}In_{0.005}Sb_{1.5}Bi_{0.49}Te_{0.01}$ bulk were loaded into a graphene die with a sandwich structure, and then sintered at 973 K for 10 min by SPS. The interface material was prepared by the ball-milling process with 304 stainless steel powder and Mg turning. The obtained sandwich-structure joints were ground, polished and then cut into dice for energy efficiency measurement. For the two-pair modules, the n-type legs were prepared with the same process as the single-leg module. The MgCuSb was selected to be the contact layer to prepare p-type legs by one-step SPS sintering. The dimension was 3.8 mm × 3.8 mm × 6 mm of the n-type and p-type legs, and the length of the thermoelectric materials and contact layer were 5 mm and 0.5 mm, respectively. The two-couple n-type and p-type legs were alternately put onto the Cu substrate with the dimensions of 10 mm × 10 mm × 0.6 mm, which has two printed Cu patterns with 0.21 mm onto the heat-conducting polymer film. The liquid In-Ga eutectic alloy was used to connect the legs and Cu electrodes to reduce thermal and electrical resistance. The Cu leading wires were soldered to the cold-side Cu electrodes to measure the current and voltage.

The fabricated module was mounted between ceramic plates, thermal grease and graphite sheets to reduce the thermal contact resistance. The electrical output power and generation performance of the fabricated module were characterized using a commercial apparatus (Mini-PEM, ADVANCE RIKO, Japan). A uniaxial pressure of 0.5 MPa was applied by Mini-PEM to reduce the electrical and thermal contact resistances. The hot-side temperature T_h of the modules was controlled by a heater, and the cold-side temperature T_c was maintained by the flowing water. In order to present widely comparable results of the performance of the module, we have utilized the Mini-PEM system where the cold-side is actively cooled and thereby the temperature difference can be accurately controlled, however, in real-world applications, suitable heat sinks need to be used to create temperature difference based on the specific application situation[82,83]. The output power (P) and cold-side heat flow (Q_c) were measured by Mini-PEM, so the energy conversion efficiency could be calculated by $\eta = \frac{P}{P+Q_c}$. The three-dimensional finite-element simulations of power-generation was performed with COMSOL Multiphysics® software in the Heat Transfer Module, and the electrical and thermal contact resistance between the multiple interfaces of the module are not considered in the simulation.

Data availability

All data generated or analyzed during this study are included in the published article and its Supplementary Information. The data that support the findings of this study are available from the corresponding author upon request.

References

1. Mori, T. & Priya, S. Materials for energy harvesting: At the forefront of a new wave. *MRS Bull.* **43**, 176–180 (2018).
2. Mao, J. et al. Advances in thermoelectrics. *Adv. Phys.* **67**, 69–147 (2018).
3. Hendricks, T., Caillat, T. & Mori, T. Keynote review of latest advances in thermoelectric generation materials, devices, and technologies 2022. *Energies* **15**, 7307 (2022).
4. Shi, X. L., Zou, J. & Chen, Z. G. Advanced thermoelectric design: from materials and structures to devices. *Chem. Rev.* **120**, 7399–7515 (2020).
5. Snyder, G. J. & Toberer, E. S. Complex thermoelectric materials. *Nat. Mater.* **7**, 105–114 (2008).
6. Zhu, T. et al. Compromise and synergy in high-efficiency thermoelectric materials. *Adv. Mater.* **29**, 1605884 (2017).
7. Tang, J. et al. Manipulation of band structure and interstitial defects for improving thermoelectric SnTe. *Adv. Funct. Mater.* **28**, 1803586 (2018).
8. Dong, J. et al. Medium-temperature thermoelectric GeTe: Vacancy suppression and band structure engineering leading to high performance. *Energy Environ. Sci.* **12**, 1396–1403 (2019).
9. Liu, Z., Sato, N., Guo, Q., Gao, W. & Mori, T. Shaping the role of germanium vacancies in germanium telluride: Metastable cubic structure stabilization, band structure modification, and stable n-type conduction. *NPG Asia Mater.* **12**, 66 (2020).
10. Mori, T. Novel principles and nanostructuring methods for enhanced thermoelectrics. *Small* **13**, 1702013 (2017).
11. Li, J.-F., Liu, W.-S., Zhao, L.-D. & Zhou, M. High-performance nanostructured thermoelectric materials. *NPG Asia Mater.* **2**, 152–158 (2010).
12. Poudel, B. et al. High-thermoelectric performance of nanostructured bismuth antimony telluride bulk alloys. *Science* **320**, 634–638 (2008).
13. Khan, A. U. et al. Nano-micro-porous skutterudites with 100% enhancement in ZT for high performance thermoelectricity. *Nano Energy* **31**, 152–159 (2017).
14. Jiang, B. et al. High figure-of-merit and power generation in high-entropy GeTe-based thermoelectrics. *Science* **377**, 208–213 (2022).
15. Liu, C. et al. Charge transfer engineering to achieve extraordinary power generation in GeTe-based thermoelectric materials. *Sci. Adv.* **9**, eadh0713 (2023).
16. Biswas, K. et al. High-performance bulk thermoelectrics with all-scale hierarchical architectures. *Nature* **489**, 414–418 (2012).
17. Roychowdhury, S. et al. Enhanced atomic ordering leads to high thermoelectric performance in $AgSbTe_2$. *Science* **371**, 722–727 (2021).
18. Su, L. et al. High thermoelectric performance realized through manipulating layered phonon-electron decoupling. *Science* **375**, 1385–1389 (2022).
19. Shang, H. et al. N-type $Mg_3Sb_{2-x}Bi_x$ alloys as promising thermoelectric materials. *Research* **2020**, 1219461 (2020).
20. Li, A., Fu, C., Zhao, X. & Zhu, T. High-performance $Mg_3Sb_{2-x}Bi_x$ thermoelectrics: progress and perspective. *Research* **2020**, 1934848 (2020).
21. Tamaki, H., Sato, H. K. & Kanno, T. Isotropic conduction network and defect chemistry in $Mg_{3+\delta}Sb_2$-based layered Zintl compounds with high thermoelectric performance. *Adv. Mater.* **28**, 10182–10187 (2016).
22. Liu, Z. et al. Demonstration of ultrahigh thermoelectric efficiency of ~7.3% in Mg_3Sb_2/MgAgSb module for low-temperature energy harvesting. *Joule* **5**, 1196–1208 (2021).
23. Chen, X. et al. Extraordinary thermoelectric performance in n-type manganese doped Mg_3Sb_2 Zintl: High band degeneracy, tuned carrier scattering mechanism and hierarchical microstructure. *Nano Energy* **52**, 246–255 (2018).
24. Shuai, J. et al. Tuning the carrier scattering mechanism to effectively improve the thermoelectric properties. *Energy Environ. Sci.* **10**, 799–807 (2017).
25. Mao, J. et al. Manipulation of ionized impurity scattering for achieving high thermoelectric performance in n-type Mg_3Sb_2-based materials. *Proc. Natl. Acad. Sci. USA* **114**, 10548–10553 (2017).
26. Kanno, T. et al. High-density Frenkel defects as origin of n-type thermoelectric performance and low thermal conductivity in Mg_3Sb_2-based materials. *Adv. Funct. Mater.* **31**, 2008469 (2021).
27. Jia, J. et al. Revealing the defect-dominated electron scattering in Mg_3Sb_2-based thermoelectric materials. *Research* **2022**, 9875329 (2022).
28. Garmroudi, F. et al. Anderson transition in stoichiometric Fe_2VAl: high thermoelectric performance from impurity bands. *Nat. Commun.* **13**, 3599 (2022).
29. Agne, M. T. et al. Disorder-induced Anderson-like localization for bidimensional thermoelectrics optimization. *Matter* **4**, 2970–2984 (2021).
30. Lei, J. et al. Efficient lanthanide Gd doping promoting the thermoelectric performance of Mg_3Sb_2-based materials. *J. Mater. Chem. A* **9**, 25944–25953 (2021).
31. Li, J.-W. et al. Bi-deficiency leading to high-performance in $Mg_3(Sb,Bi)_2$-based thermoelectric materials. *Adv. Mater.* **35**, e2209119 (2023).
32. Yin, L. et al. Reliable n-type $Mg_{3.2}Sb_{1.5}Bi_{0.49}Te_{0.01}$/304 stainless steel junction for thermoelectric applications. *Acta Mater.* **198**, 25–34 (2020).
33. Cheng, K. et al. Efficient $Mg_2Si_{0.3}Sn_{0.7}$ thermoelectrics demonstrated for recovering heat of about 600 K. *Mater. Today Phys.* **28**, 100887 (2022).
34. Lou, L.-Y. et al. Tunable electrical conductivity and simultaneously enhanced thermoelectric and mechanical properties in n-type Bi_2Te_3. *Adv. Sci.* **9**, 2203250 (2022).
35. Deng, P.-Y., Wang, K.-K., Sung, H.-Y., Wu, W.-W. & Wu, H.-J. Liquid-like copper chalcogenide modulates electron donors in high-performance n-type PbTe thermoelectrics. *Cell Rep. Phys. Sci.* **4**, 101413 (2023).
36. Wu, X. et al. Interface engineering boosting high power density and conversion efficiency in $Mg_2Sn_{0.75}Ge_{0.25}$-based thermoelectric devices. *Adv. Energy Mater.* **13**, 2301350 (2023).
37. Zhan, S. et al. Realizing high-ranged thermoelectric performance in $PbSnS_2$ crystals. *Nat. Commun.* **13**, 5937 (2022).
38. Deng, R. et al. High thermoelectric performance in $Bi_{0.46}Sb_{1.54}Te_3$ nanostructured with ZnTe. *Energy Environ. Sci.* **11**, 1520–1535 (2018).
39. Hao, F. et al. High efficiency Bi_2Te_3-based materials and devices for thermoelectric power generation between 100 and 300 °C. *Energy Environ. Sci.* **9**, 3120–3127 (2016).
40. Yin, L. et al. Low-temperature sintering of Ag nanoparticles for high-performance thermoelectric module design. *Nat. Energy* **8**, 665–674 (2023).
41. Kanno, T. et al. Enhancement of average thermoelectric figure of merit by increasing the grain-size of $Mg_{3.2}Sb_{1.5}Bi_{0.49}Te_{0.01}$. *Appl. Phys. Lett.* **112**, 033903 (2018).
42. Luo, T. et al. Nb-mediated grain growth and grain-boundary engineering in Mg_3Sb_2-based thermoelectric materials. *Adv. Funct. Mater.* **31**, 2100258 (2021).
43. Wang, L. et al. Realizing high thermoelectric performance in n-type $Mg_3(Sb, Bi)_2$-based materials via synergetic Mo addition and Sb–Bi ratio refining. *Adv. Energy Mater.* **13**, 2301667 (2023).
44. Kuo, J. J. et al. Grain boundary dominated charge transport in Mg_3Sb_2-based compounds. *Energy Environ. Sci.* **11**, 429–434 (2018).
45. Ohno, S. et al. Phase boundary mapping to obtain n-type Mg_3Sb_2-based thermoelectrics. *Joule* **2**, 141–154 (2018).

46. Shuai, J. et al. Significant role of Mg stoichiometry in designing high thermoelectric performance for $Mg_3(Sb, Bi)_2$-based n-type Zintls. *J. Am. Chem. Soc.* **140**, 1910–1915 (2018).
47. Mott, N. F. Conduction in glasses containing transition metal ions. *J. Non·Cryst. Solids* **1**, 1–17 (1968).
48. Sussardi, A., Tanaka, T., Khan, A. U., Schlapbach, L. & Mori, T. Enhanced thermoelectric properties of samarium boride. *J. Materiomics* **1**, 196–204 (2015).
49. Zvyagin, I. P. On the theory of hopping transport in disordered semiconductors. *Phys. Status Solidi B* **58**, 443–449 (1973).
50. Mori, T. & Tanaka, T. Effect of transition metal doping and carbon doping on thermoelectric properties of YB_{66} single crystals. *J. Solid State Chem.* **179**, 2889–2894 (2006).
51. Zhang, J., Song, L. & Iversen, B. B. Probing efficient n-type lanthanide dopants for Mg_3Sb_2 thermoelectrics. *Adv. Sci.* **7**, 2002867 (2020).
52. Pan, Y. et al. $Mg_3(Bi,Sb)_2$ single crystals towards high thermoelectric performance. *Energy Environ. Sci.* **13**, 1717–1724 (2020).
53. Gorai, P., Ortiz, B. R., Toberer, E. S. & Stevanović, V. Investigation of n-type doping strategies for Mg_3Sb_2. *J. Mater. Chem. A* **6**, 13806–13815 (2018).
54. Chen, Q. et al. The mechanisms of grain growth of Mg alloys: a review. *J. Magnes. Alloy.* **10**, 2384–2397 (2022).
55. Basu, I., Pradeep, K. G., Mießen, C., Barrales-Mora, L. A. & Al-Samman, T. The role of atomic scale segregation in designing highly ductile magnesium alloys. *Acta Mater.* **116**, 77–94 (2016).
56. Sepehri-Amin, H., Imasato, K., Wood, M., Kuo, J. J. & Snyder, G. J. Evolution of nanometer-scale microstructure within grains and in the intergranular region in thermoelectric $Mg_3(Sb,Bi)_2$ alloys. *ACS Appl. Mater. Interfaces* **14**, 37958–37966 (2022).
57. Shu, R. et al. Solid-state Janus nanoprecipitation enables amorphous-like heat conduction in crystalline Mg_3Sb_2-based thermoelectric materials. *Adv. Sci.* **9**, e2202594 (2022).
58. Lin, Y. C. et al. Scanning moiré fringe method: a superior approach to perceive defects, interfaces, and distortion in 2D materials. *ACS Nano* **14**, 6034–6042 (2020).
59. Ke, X., Zhang, M., Zhao, K. & Su, D. Moiré fringe method via scanning transmission electron microscopy. *Small Methods* **6**, e2101040 (2022).
60. Hÿtch M. J., Snoeck E. & Kilaas R. Quantitative measurement of displacement and strain fields from HREM micrographs. *Ultramicroscopy* **74**, 131–146 (1998).
61. Li, J.-W. et al. Wide-temperature-range thermoelectric n-type $Mg_3(Sb,Bi)_2$ with high average and peak *zT* values. *Nat. Commun.* **14**, 7428 (2023).
62. Kim, H.-S., Gibbs, Z. M., Tang, Y., Wang, H. & Snyder, G. J. Characterization of Lorenz number with Seebeck coefficient measurement. *APL Mater.* **3**, 041506 (2015).
63. Imasato, K., Ohno, S., Kang, S. D. & Snyder, G. J. Improving the thermoelectric performance in $Mg_{3+x}Sb_{1.5}Bi_{0.49}Te_{0.01}$ by reducing excess Mg. *APL Mater.* **6**, 016106 (2018).
64. Zhang, J., Song, L., Mamakhel, A., Jørgensen, M. R. V. & Iversen, B. B. High-performance low-cost n-type Se-doped Mg_3Sb_2-based Zintl compounds for thermoelectric application. *Chem. Mater.* **29**, 5371–5383 (2017).
65. Zhang, J., Song, L. & Iversen, B. B. Rapid one-step synthesis and compaction of high-performance n-type Mg_3Sb_2 thermoelectrics. *Angew. Chem. Int. Ed.* **59**, 4278–4282 (2020).
66. Li, J. et al. The manipulation of substitutional defects for realizing high thermoelectric performance in Mg_3Sb_2-based Zintl compounds. *J. Mater. Chem. A* **7**, 19316–19323 (2019).
67. Cahill, D. G., Watson, S. K. & Pohl, R. O. Lower limit to the thermal conductivity of disordered crystals. *Phys. Rev. B* **46**, 6131–6140 (1992).
68. Agne, M. T., Hanus, R. & Snyder, G. J. Minimum thermal conductivity in the context of diffuson-mediated thermal transport. *Energy Environ. Sci.* **11**, 609–616 (2018).
69. Clarke, D. Materials selection guidelines for low thermal conductivity thermal barrier coatings. *Surf. Coat. Technol.* **163**, 67–74 (2003).
70. Callaway, J. & von Baeyer, H. C. Effect of point imperfections on lattice thermal conductivity. *Phys. Rev.* **120**, 1149–1154 (1960).
71. Klemens, P. G. Thermal resistance due to point defects at high temperatures. *Phys. Rev.* **119**, 507–509 (1960).
72. Li, G., Wang, Q., Cui, Z. & Guo, R. Competition between intrinsic and extrinsic phonon scatterings in cubic BP and BAs with point defects. *Phys. Rev. B* **107**, 184118 (2023).
73. Agne, M. T. et al. Heat capacity of Mg_3Sb_2, Mg_3Bi_2, and their alloys at high temperature. *Mater. Today Phys.* **6**, 83–88 (2018).
74. Peng, W., Petretto, G., Rignanese, G.-M., Hautier, G. & Zevalkink, A. An unlikely route to low lattice thermal conductivity: Small atoms in a simple layered structure. *Joule* **2**, 1879–1893 (2018).
75. Ding, J. et al. Soft anharmonic phonons and ultralow thermal conductivity in $Mg_3(Sb,Bi)_2$ thermoelectrics. *Sci. Adv.* **7**, eabg1449 (2021).
76. Petersen, A., Bhattacharya, S., Tritt, T. M. & Poon, S. J. Critical analysis of lattice thermal conductivity of half-Heusler alloys using variations of Callaway model. *J. Appl. Phys.* **117**, 035706 (2015).
77. Ricco, S. et al. In situ strain tuning of the metal-insulator-transition of Ca_2RuO_4 in angle-resolved photoemission experiments. *Nat. Commun.* **9**, 4535 (2018).
78. Zebarjadi, M. et al. Power factor enhancement by modulation doping in bulk nanocomposites. *Nano Lett.* **11**, 2225–2230 (2011).
79. Kang, H. B. et al. Decoupled phononic-electronic transport in multiphase n-type half-Heusler nanocomposites enabling efficient high temperature power generation. *Mater. Today* **36**, 63–72 (2020).
80. Jiang, B. et al. High-entropy-stabilized chalcogenides with high thermoelectric performance. *Science* **371**, 830–834 (2021).
81. Chetty, R., Babu, J. & Mori, T. Best practices for evaluating the performance of thermoelectric devices. *Joule* **8**, 556–562 (2024).
82. Zoui, M. A., Bentouba, S., Stocholm, J. G. & Bourouis, M. A review on thermoelectric generators: progress and applications. *Energies* **13**, 3606 (2020).
83. Tohidi, F., Ghazanfari Holagh, S. & Chitsaz, A. Thermoelectric generators: a comprehensive review of characteristics and applications. *Appl. Therm. Eng.* **201**, 117793 (2022).

Acknowledgements

T.M. acknowledges financial support from the JST Mirai Program Grant Number JPMJMI19A1. Support from JSPS KAKENHI 22K14505 is also acknowledged for the TEM. We thank T.S. Suzuki of NIMS for his technical support with the thermal expansion measurement.

Author contributions

L.W. contributed to the sample preparations, characterization, data analysis, conceptualization, methodology, writing, and revising the manuscript. W.Z. contributed to data analysis, methodology, writing, and revising the manuscript. S.Y.B. contributed to data analysis, writing, and revising the manuscript. N.K. and D-H.N. contributed to the TEM characterization. T.M. led the project, providing conceptualization and supervision, writing-review and editing, and funding acquisition. All authors contributed to the review of the final manuscript.

Competing interests

T.M. and L.W. have filed one Japanese patent application (2024-082608) on the work described here. The remaining authors declare no competing interests.

Additional information

Supplementary information The online version contains supplementary material available at https://doi.org/10.1038/s41467-024-51120-3.

Correspondence and requests for materials should be addressed to Takao Mori.

Peer review information *Nature Communications* thanks the anonymous reviewer(s) for their contribution to the peer review of this work. A peer review file is available.